

# Efficient learning of quantum noise

Robin Harper,<sup>1</sup> Steven T. Flammia,<sup>1,2,3</sup> and Joel J. Wallman<sup>4,3</sup>

<sup>1</sup>*Centre for Engineered Quantum Systems, School of Physics, University of Sydney, Sydney, NSW 2006 Australia*

<sup>2</sup>*Yale Quantum Institute, Yale University, New Haven, CT 06520, USA*

<sup>3</sup>*Quantum Benchmark Inc., 100 Ahrens Street West, Suite 203, Kitchener, ON N2H 4C3, Canada*

<sup>4</sup>*Institute for Quantum Computing and Department of Applied Mathematics,  
University of Waterloo, Waterloo, Ontario N2L 3G1, Canada*

(Dated: November 27, 2021)

Noise is the central obstacle to building large-scale quantum computers. Quantum systems with sufficiently uncorrelated and weak noise could be used to solve computational problems that are intractable with current digital computers. There has been substantial progress towards engineering such systems. However, continued progress depends on the ability to characterize quantum noise reliably and efficiently with high precision. Here we introduce a protocol that completely and efficiently characterizes the error rates of quantum noise and we experimentally implement it on a 14-qubit superconducting quantum architecture. The method returns an estimate of the effective noise with relative precision and detects all correlated errors. We show how to construct a quantum noise correlation matrix allowing the easy visualization of all pairwise correlated errors, enabling the discovery of long-range two-qubit correlations in the 14 qubit device that had not previously been detected. These properties of the protocol make it exceptionally well suited for high-precision noise metrology in quantum information processors. Our results are the first implementation of a provably rigorous, full diagnostic protocol capable of being run on state of the art devices and beyond. These results pave the way for noise metrology in next-generation quantum devices, calibration in the presence of crosstalk, bespoke quantum error-correcting codes, and customized fault-tolerance protocols that can greatly reduce the overhead in a quantum computation.

Useful large-scale quantum computers will require both careful calibration to reduce errors as well as some form of error correction before scalable, universal quantum computing can be realized. Recent work has made tremendous progress in this direction [1–8]. Due to crosstalk, optimal calibrations of gates depend on the other gates that are being implemented, which can reduce the overall system error rate by an order of magnitude [9]. Furthermore, error correction routines rely on knowing what the most likely error sources are. Error correction routines that are optimized for the specific noise in a system can dramatically outperform generic ones [10, 11].

The calibration and error correction necessary for useful large-scale quantum computing therefore depends upon the ability to characterize the noise in large quantum systems. This characterization will become increasingly important as the field continues to progress [12]. Unfortunately, current methods of characterizing noise are infeasible as device sizes approach 10 or more qubits, which is already the state of the art. The question is then how to efficiently characterize the noise in these larger devices.

Here we experimentally implement a protocol that allows us to learn a complete description of the effective qubit error rates in a large-scale quantum device. The protocol is efficient in  $n$ , the number of qubits, and comes with mathematically rigorous guarantees on its convergence and performance assuming only mild and physically plausible assumptions. Furthermore, the method is immune to systematic bias due to state preparation and measurement errors (SPAM), and achieves both high precision and accuracy.

Prior work on characterizing noise in quantum devices was, by contrast, unable to achieve one or more of these desiderata. Process tomography [13] and gate set tomography [14] do not scale past a handful of qubits even when sophisticated techniques such as compressed sensing [15–17] are utilized.

Randomized benchmarking [18, 19] (RB) is a protocol that does scale in principle, but it provides only an incomplete description of the noise. Recent extensions of RB improve its scalability [20, 21] and broaden its applicability [22–25], but they still result in coarse, incomplete descriptions of the noise. Various methods of characterizing correlations based upon RB have been proposed [18, 26, 27], but none are scalable.

For any given noisy quantum system comprising  $n$  qubits, we can consider the average noise to have the special form of a Pauli channel [28]. Although not every noise channel is a Pauli channel, practical methodologies have been developed to transform the noise to be exceptionally well-approximated by a Pauli channel without introducing new errors [29, 30]. A Pauli channel  $\mathcal{E}$  acting on a quantum state  $\rho$  is of the form  $\mathcal{E}(\rho) = \sum_j p(j) P_j \rho P_j$ , where  $p(j)$  is the error rate associated with the Pauli operator  $P_j$ . The Pauli error rates  $p(j)$  form a probability distribution. These are closely related to, but distinct from, the Pauli fidelities, which are defined to be  $f(j) = 2^{-n} \text{Tr}(P_j \mathcal{E}(P_j))$ . Thus, when a state  $\rho$  is subjected to the noisy channel  $\mathcal{E}$ , the Pauli error rate  $p(j)$  describes the probability of a multi-qubit Pauli error  $P_j$  affecting the system, while the Pauli fidelity describes how faithfully a given multi-spin Pauli operator is transmitted. The Pauli error rates  $p(j)$  and fidelities  $f(j)$  are related by a Walsh-Hadamard transform. The (rescaled) average value of  $f(j)$ , which is measured by RB, is the only figure of merit estimated and reported by most quantum computing experiments.

Obtaining a complete description of the Pauli error rates requires learning more than just the single-Pauli fidelities or single-Pauli error rates [31], i.e., those associated with the single-qubit Pauli operators such as  $\sigma_z^{(1)}$  or  $\sigma_x^{(3)}$ . We must learn all of the noise correlations in the system, including those associated with multi-qubit Pauli operators, e.g.,

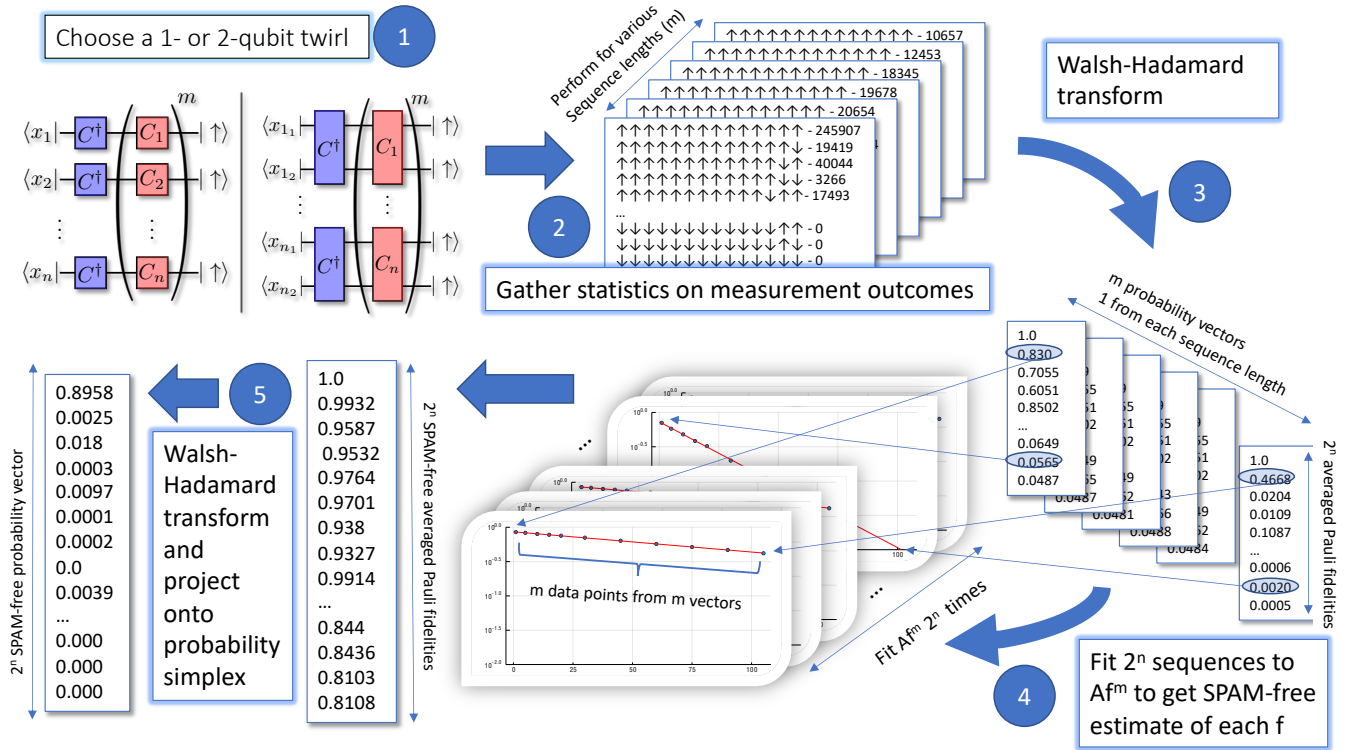


FIG. 1. An illustration of our protocol for characterizing the entire averaged probability vector for an  $n$ -qubit device. In step 1 we determine whether we wish to examine the correlations between qubits activated in single-qubit mode or when gates between the qubits are also used. Each red box in the quantum circuits of step 1 denotes a random Clifford gate, and the circuits themselves are run for varying lengths  $m$  (with time moving from right to left). The final gate  $C^\dagger$  is not random, but is rather an inversion gate returning the system to its initial state in the ideal case. Step 2 gathers output statistics from the measurement results  $x_i$  obtained in the experiments in step 1, and the empirically estimated probability distributions for these outcomes are transformed in Step 3 via a Walsh-Hadamard transform. The transformed values are each fit to an exponential decay in Step 4, allowing us to reconstruct the Pauli fidelities free of state preparation and measurement error (SPAM). With a final reverse transformation in Step 5, we reconstruct the entire list of effective qubit error rates.

$\sigma_z^{(1)} \otimes \mathbb{1}^{(2)} \otimes \sigma_x^{(3)}$ . Knowing these correlations is essential for removing unwanted correlated errors [26] and for performing optimal quantum error correction [32]. The number of all possible noise correlations grows exponentially with the number of qubits, so it is furthermore crucial to have an efficient description of these correlations in order to focus error-mitigation efforts on the most dominant noise sources.

Figure 1 gives a complete description of our protocol for learning quantum noise. It proceeds in five steps: First choose a number of long sequences of random quantum gates chosen independently from the single-qubit (or two-qubit) Clifford group, i.e., the group generated by the Hadamard, Phase, and (for two-qubits) CNOT gates on each individual qubit or qubit pair. Then estimate the resulting empirical probability distribution over the measurement outcomes and take a Walsh-Hadamard transform of the result. The resulting values will exhibit an exponential decay with respect to the sequence length parameter,  $m$ , so in step 4 we fit to such a model to learn the decay constants. Finally, we transform back and project onto the probability simplex.

This procedure provably converges to an estimate of the probability distribution of the average noise in the system [33], though the variant implemented here uses random

gates chosen from the single-qubit Clifford group instead of the Pauli group. This leads to a simpler protocol, but one that additionally averages over the local basis information. Averaging the noise in this way reduces the number of parameters that need to be reconstructed from  $4^n$  to  $2^n$ . We call this reduced distribution the qubit error rates to contrast with the larger distribution of Pauli error rates, and we similarly define the set of  $2^n$  qubit fidelities in analogy with the  $4^n$  Pauli fidelities. Importantly, the qubit error rates are still capable of describing all many-body correlations in the noise.

This protocol compares favorably to recent extensions of RB such as cycle benchmarking [25], character benchmarking [24], and correlation benchmarking [27]. Rather than estimating individual average fidelities one at a time, it can estimate all of them simultaneously.

The protocol presented in Figure 1 reconstructs the full probability distribution with a number of experiments that scales polynomially in the number of qubits  $n$ , but requires computational resources that scale polynomially with the number of error rates to be estimated. The number of qubit error rates scales as  $2^n$ , so to make our protocol truly scalable, we need a method to estimate an efficient description of the noise that nonetheless captures the correlations in a trans-

parent, systematic, and physically motivated way.

To achieve an efficient protocol, scaling polynomially in  $n$ , we introduce the notion of a *Gibbs random field* to describe the error rates  $p(j)$ . A Gibbs random field (GRF) is a strictly positive probability distribution that obeys certain conditional independence properties known as Markov conditions, defined below. These conditions restrict the range of possible correlations enough to make the problem of noise characterization tractable, but they allow sufficient expressive power that a GRF can accurately model noise in real devices.

Associated to any GRF is a factorization of the error rates into a product of factors, where each factor is a positive function depending only on a subset of the qubits. The *factor graph* of this factorization, depicted in Figure 2, has two types of nodes: one set for the random variables associated to each single-qubit error, and one set for each factor in the factorization of  $p$ , with factor nodes connected to exactly the qubit nodes they depend on. We say that two single-qubit nodes are adjacent if they connect to some common factor. The Markov conditions then say that the correlations in a GRF are of a specific form: errors on any subset of non-adjacent qubits are conditionally independent given the errors on their neighbors.

When quantum noise is approximated by a GRF, the parameters of the GRF can be learned efficiently, precisely, and accurately by only estimating the marginal distributions on the factors and their neighbors. When the factors have a small bounded size, then the protocol detailed in Figure 1 performs this estimation with aplomb. The specific methodology for estimating the global probability distribution as a GRF from the estimated marginals is discussed in the Appendices. Note that it is not necessary to know the topology of the GRF factor graph in advance, and we will show how to learn this in future work.

Our first experiments were run using the single-qubit protocol on the 14-qubit superconducting quantum architecture *Melbourne*, made available by IBM through the IQX online quantum computing environment [34]. After completion of stage 4 of the protocol, we had reconstructed the entire averaged noise on the machine, returning all the qubit fidelities with multiplicative precision.

The real utility of the protocol then comes from its unique ability to reconstruct the SPAM-free qubit error rates. This allows us to utilize the standard tools for analyzing probability distributions to understand the noise correlations in the device. Indeed, any functional of the reconstructed probability distribution can be computed from the data, such as the mutual information between pairs of qubits, the covariance matrix of the errors, or the correlation matrix (as in Figure 2 or Figure 3). In particular, the covariance and correlation matrices can be computed unconditionally in polynomial time irrespective of any efficient GRF description by using our protocol (see Appendix D). These tools provide invaluable diagnostic information about correlated errors that is difficult or impossible to obtain using prior art.

Of critical importance in developing error-corrected quantum devices will be the identification and elimination of long-range qubit correlations. Our protocol allows such correlations to be identified and quantified. A GRF model that en-

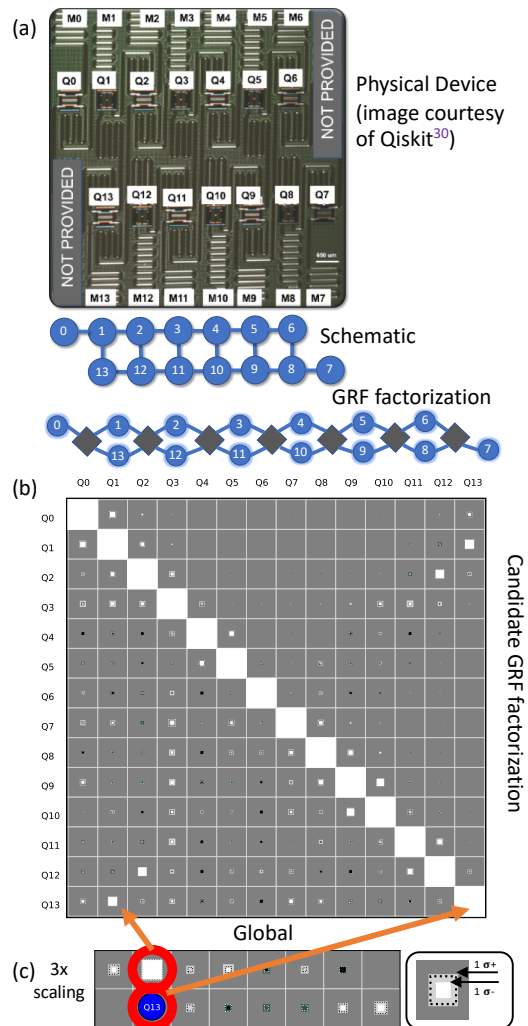


FIG. 2. (a) Spatial layout of the qubits in the 14 qubit *Melbourne* architecture. Edges in the schematic graph correspond to qubit pairs that can be coupled via a two-qubit gate. The factor graph below that is for a Gibbs random field (GRF) that models quantum noise via spatially local correlations in the device. Each diamond-shaped node is a factor that can describe arbitrary couplings among its constituent qubits. (b) The correlation matrix of the globally estimated distribution. Correlation matrices (see Appendix A) are always symmetric, so we plot separately the correlation in the global reconstruction (lower left) and the GRF reconstruction (upper right) assuming the factor graph in (a). Gray background indicates a value of zero, and white (black) boxes indicate positive (negative) values between  $[-1, 1]$  in proportion to their relative area. (c) An example of how the spatial correlation of the qubits on the device translate to the layout in the correlation matrix. This example shows that although qubit 1 and qubit 13 are spatially adjacent, they are not adjacent in the matrix. To the right, we illustrate the convention used to indicate error bars, using here  $1\sigma$  bounds.

forces short-range correlations can be constructed using the topology of the connections for the device in question. Reconstructing the observed probability distribution within the ansatz of the GRF allows two candidate distributions with different locality of their noise to be compared using metrics

## Two-qubit protocol

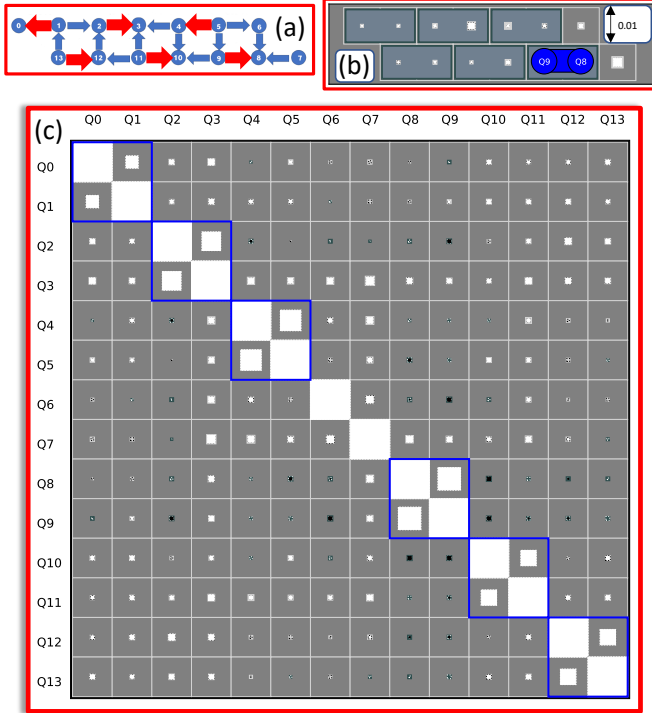


FIG. 3. (a) The two-qubit protocol requires the qubits on the device to be partitioned into disjoint sets of one or two qubits. Here we present one of the distinct partitionings used in the experiments. Other partitionings are discussed in the appendix. (b) The mutual information returned by the protocol. The chart shown is a Hinton diagram, laid out to reflect the physical layout of the device. The mutual information between a qubit and the qubit pair Q8 and Q9 is shown as a white square, the area of which is proportional to the value. A full square represents a value of 0.01 Shannons ( $= \text{bits} \times \ln 2$ ). By treating the qubit pair as a single qubit we remove the mutual information between the paired qubits, allowing us to see the mutual information captured between the qubit pair and the other qubits. The qubit pairings are indicated with blue shading. As can be seen there is significant mutual information between qubit 3 and this particular qubit pair. This type of correlation is longer than nearest-neighbor and would be difficult to detect with previous protocols. (c) The correlation matrix corresponding to the distinct qubit-pair groupings shown in (a). The blue boxes show the qubit couplings, and would be expected to reflect the spread of errors between the two-qubit gates. While there are a number of long-range interactions that are significant, it is easy to identify that the errors on qubit 3 positively correlate with the errors on each other qubit.

such as the Jensen-Shannon distance (JSD) between the distributions (see Appendix A). If two candidate distributions  $p(j)$  and  $q(j)$  for describing the noise in the device have different factor topologies, but are close in JSD, then the model with more elaborate connections is likely overfitting to the data, and we can safely reject the additional correlations that the model represents as potential factors. In this way, multiple reconstructions can allow us to test for specific correlations that may or may not be present in the device.

Figure 2 illustrates the information that can be learned from

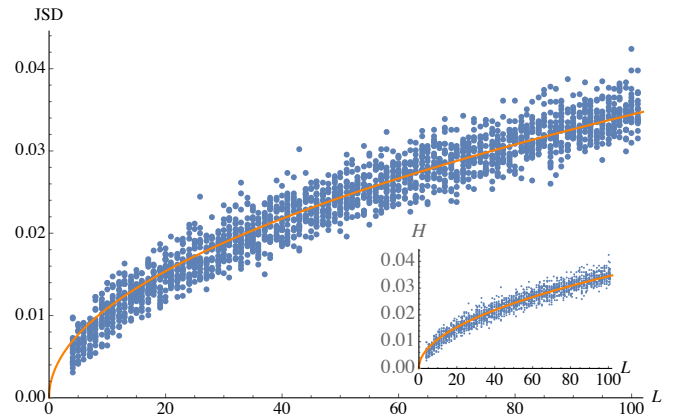


FIG. 4. The Jensen-Shannon distance (JSD) and Hellinger distance ( $H$ ) (see Appendix A for definitions) for comparing the true ( $p$ ) and estimated ( $q$ ) probability distribution of Pauli errors on a chain of length  $L$  for  $L \leq 100$ , with 20 random instances per value of  $L$ . The simulated noise is modeled by nearest-neighbor correlations in some true distribution  $p$ , and the estimate is reconstructed using the method in the text by estimating local marginal probability distributions to build a global estimate  $q$  in a factorized form. Each local marginal was estimated using a constant number of samples, independent of  $L$ , so that the growth in the error with  $L$  measures how global noise reconstruction accuracy degrades when the accuracy of the local estimates is fixed. The orange fit lines are the result of single-parameter least-squares fits to the model  $a\sqrt{x}$ . The good qualitative agreement indicates that errors from local statistical fluctuations add up incoherently rather than constructively.

the probability distribution, the construction of a short-range GRF model for the noise and the comparison of the GRF model to the global estimated distribution. In this case we calculated the JSD to be 0.035(4), demonstrating that when the device is operated using only single-qubit gates the long-range qubit correlations are small for these operations. This is an important fact when considering such things as error correction and helps explain recent successful demonstrations of important elements of fault tolerance on the device [35].

The two-qubit protocol, which activates resonators simultaneously between qubit pairs, unsurprisingly gives an entirely different characterization of the device. With the two-qubit protocol it is anticipated that the two-qubit gate will spread errors between each pair of qubits. This will lead to strong mutual information between qubits in each pair, which will tend to swamp any other smaller signals. However, by treating these qubits as a unified pair (i.e. a single random variable) we can calculate metrics such as the mutual information between the qubit pair and other qubits (or pairs of qubits). This is illustrated in Figure 3.

As could be anticipated by the correlation matrices in Figure 3, the JSD between the probability distribution measured using the the two-qubit protocol and the local GRF model has increased by almost an order of magnitude to 0.265(1). While *unknown* correlations would adversely affect the performance of error correction routines on the device, here we have fully calculated the averaged noise afflicting the system. This will allow tailored decoders to be constructed that can utilize the

noise profile to increase the probability of successfully decoding error syndromes. These correlations also provide valuable diagnostic information that can be used to learn the microscopic origin of the noise and potentially mitigate the source of the errors.

Finally, while the experiments here show the efficacy of this protocol on 14 qubits, our numerical simulations confirm the accuracy with which the protocol reconstructs the global estimates on much larger systems. In Figure 4 we present a numerical simulation demonstrating the accuracy of the protocol in reconstructing a GRF for a system with up to 100 qubits in a line by measuring few-body marginal distributions with a fixed number of samples. The size of the simulated systems is far beyond what any other method is currently capable of characterizing. The appendices contain more examples of simulations showing that the methodologies discussed here are indeed accurate and scalable. Mathematical proofs that provide recovery guarantees up to relative precision using this protocol are published in a separate paper [33]. These results also prove that, subject to mild caveats, this protocol runs in polynomial time in the number of qubits.

Our experiments give the first demonstration of a protocol

that is practical, relevant, and immediately applicable to characterizing error rates and correlated errors in present-day devices with a large ( $>10$ ) number of qubits. This protocol opens myriad opportunities for novel diagnostic tools and practical applications. For example, structure learning techniques can be applied to learn the most accurate and efficient GRF noise model that describes the error rates. In addition to the applications mentioned in the abstract, machine learning for fine-tuned error-correction decoders using the actual noise map of the device, quantum control for optimal gate synthesis, and noise-aware circuit compiling techniques are just some of the applications of this new method for characterizing quantum noise.

**Acknowledgements.** We thank S. Bartlett, A. Doherty, and T. Monz for comments on an earlier draft. This work was supported in part by the US Army Research Office grant numbers W911NF-14-1-0098 and W911NF-14-1-0103, the Australian Research Council Centre of Excellence for Engineered Quantum Systems (EQUS) CE170100009, the Government of Ontario, and the Government of Canada through the Canada First Research Excellence Fund (CFREF) and Transformative Quantum Technologies (TQT), the Natural Sciences and Engineering Research Council (NSERC), Industry Canada.

- 
- [1] P. Schindler, J. T. Barreiro, T. Monz, V. Nebendahl, D. Nigg, M. Chwalla, M. Hennrich, and R. Blatt, *Science* **332**, 1059 (2011).
- [2] M. D. Reed, L. DiCarlo, S. E. Nigg, L. Sun, L. Frunzio, S. M. Girvin, and R. J. Schoelkopf, *Nature* **482**, 382 (2012), arXiv:1109.4948.
- [3] R. Barends, J. Kelly, A. Megrant, A. Veitia, D. Sank, E. Jeffrey, T. C. White, J. Mutus, A. G. Fowler, B. Campbell, Y. Chen, Z. Chen, B. Chiaro, A. Dunsworth, C. Neill, P. O'Malley, P. Roushan, A. Vainsencher, J. Wenner, A. N. Korotkov, A. N. Cleland, and J. M. Martinis, *Nature* **508**, 500 (2014), arXiv:1402.4848.
- [4] D. Nigg, M. Müller, E. A. Martinez, P. Schindler, M. Hennrich, T. Monz, M. A. Martin-Delgado, and R. Blatt, *Science* **345**, 302 (2014), arXiv:1403.5426.
- [5] J. Kelly, R. Barends, A. G. Fowler, A. Megrant, E. Jeffrey, T. C. White, D. Sank, J. Y. Mutus, B. Campbell, Y. Chen, Z. Chen, B. Chiaro, A. Dunsworth, I.-C. Hoi, C. Neill, P. J. J. O'Malley, C. Quintana, P. Roushan, A. Vainsencher, J. Wenner, A. N. Cleland, and J. M. Martinis, *Nature* **519**, 66 (2015), arXiv:1411.7403.
- [6] A. D. Córcoles, E. Magesan, S. J. Srinivasan, A. W. Cross, M. Steffen, J. M. Gambetta, and J. M. Chow, *Nat Comms* **6**, 6979 (2015), arXiv:1410.6419.
- [7] N. Ofek, A. Petrenko, R. Heeres, P. Reinhold, Z. Leghtas, B. Vlastakis, Y. Liu, L. Frunzio, S. M. Girvin, L. Jiang, M. Mirrahimi, M. H. Devoret, and R. J. Schoelkopf, *Nature* **536**, 441 (2016), arXiv:1602.04768.
- [8] N. M. Linke, M. Gutierrez, K. A. Landsman, C. Figgatt, S. Debnath, K. R. Brown, and C. Monroe, *Science Advances* **3**, e1701074 (2017), arXiv:1611.06946.
- [9] C. Neill, P. Roushan, K. Kechedzhi, S. Boixo, S. V. Isakov, V. Smelyanskiy, A. Megrant, B. Chiaro, A. Dunsworth, K. Arya, R. Barends, B. Burkett, Y. Chen, Z. Chen, A. Fowler, B. Foxen, M. Giustina, R. Graff, E. Jeffrey, T. Huang, J. Kelly, P. Klimov, E. Lucero, J. Mutus, M. Neeley, C. Quintana, D. Sank, A. Vainsencher, J. Wenner, T. C. White, H. Neven, and J. M. Martinis, *Science* **360**, 195 (2018).
- [10] P. Aliferis and J. Preskill, *Phys. Rev. A* **78**, 052331 (2008), arXiv:0710.1301.
- [11] D. K. Tuckett, S. D. Bartlett, and S. T. Flammia, *Phys. Rev. Lett.* **120**, 050505 (2018), arXiv:1708.08474.
- [12] J. M. Martinis, *npj Quantum Information* **1**, (2015), arXiv:1510.01406.
- [13] I. L. Chuang and M. A. Nielsen, *J. Mod. Opt.* **44**, 2455 (1997), quant-ph/9610001.
- [14] R. Blume-Kohout, J. K. Gamble, E. Nielsen, K. Rudinger, J. Mizrahi, K. Fortier, and P. Maunz, *Nature Communications* **8**, (2016), arXiv:1605.07674.
- [15] D. Gross, Y.-K. Liu, S. T. Flammia, S. Becker, and J. Eisert, *Phys. Rev. Lett.* **105**, 150401 (2010), arXiv:0909.3304.
- [16] S. T. Flammia, D. Gross, Y.-K. Liu, and J. Eisert, *New J. Phys.* **14**, 095022 (2012), arXiv:1205.2300.
- [17] C. A. Ríofrío, D. Gross, S. T. Flammia, T. Monz, D. Nigg, R. Blatt, and J. Eisert, *Nature Communications* **8**, 15305 (2017).
- [18] J. Emerson, R. Alicki, and K. Życzkowski, *J. Opt. B* **7**, S347 (2005), quant-ph/0503243.
- [19] E. Knill, D. Leibfried, R. Reichle, J. Britton, R. B. Blakestad, J. D. Jost, C. Langer, R. Ozeri, S. Seidelin, and D. J. Wineland, *Phys. Rev. A* **77**, 012307 (2008), arXiv:0707.0963.
- [20] D. S. França and A. K. Hashagen, *Journal of Physics A: Mathematical and Theoretical* **51**, 395302 (2018), arXiv:1803.03621.
- [21] T. J. Proctor, A. Carignan-Dugas, K. Rudinger, E. Nielsen, R. Blume-Kohout, and K. Young, arXiv e-prints, arXiv:1807.07975 (2018), arXiv:1807.07975 [quant-ph].
- [22] S. Kimmel, M. P. da Silva, C. A. Ryan, B. R. Johnson, and T. Ohki, *Phys. Rev. X* **4**, 011050 (2014), arXiv:1306.2348.

- [23] J. Wallman, C. Granade, R. Harper, and S. T. Flammia, *New Journal of Physics* **17**, 113020 (2015).
- [24] J. Helsen, X. Xue, L. M. Vandersypen, and S. Wehner, (2018), [arXiv:1806.02048](#).
- [25] A. Erhard, J. J. Wallman, L. Postler, M. Meth, R. Stricker, E. A. Martinez, P. Schindler, T. Monz, J. Emerson, and R. Blatt, *arXiv e-prints*, [arXiv:1902.08543](#) (2019), [arXiv:1902.08543 \[quant-ph\]](#).
- [26] J. M. Gambetta, A. D. Córcoles, S. T. Merkel, B. R. Johnson, J. A. Smolin, J. M. Chow, C. A. Ryan, C. Rigetti, S. Poletto, T. A. Ohki, M. B. Ketchen, and M. Steffen, *Physical Review Letters* **109**, 240504 (2012), [arXiv:1204.6308](#).
- [27] D. C. McKay, S. Sheldon, J. A. Smolin, J. M. Chow, and J. M. Gambetta, *Physical Review Letters* **122**, 200502 (2019).
- [28] E. Knill, *Nature* **434**, 39 (2005), [arXiv:quant-ph/0410199](#).
- [29] J. J. Wallman and J. Emerson, *Phys. Rev. A* **94**, 052325 (2016), [arXiv:1512.01098](#).
- [30] M. Ware, G. Ribeill, D. Riste, C. A. Ryan, B. Johnson, and M. P. da Silva, (2018), [1803.01818](#).
- [31] K. Wright, K. M. Beck, S. Debnath, J. M. Amini, Y. Nam, N. Grzesiak, J. S. Chen, N. C. Panti, M. Chmielewski, C. Collins, K. M. Hudek, J. Mizrahi, J. D. Wong-Campos, S. Allen, J. Apisdorf, P. Solomon, M. Williams, A. M. Ducore, A. Blinov, S. M. Kreikemeier, V. Chaplin, M. Keesan, C. Monroe, and J. Kim, *arXiv e-prints*, [arXiv:1903.08181](#) (2019), [arXiv:1903.08181 \[quant-ph\]](#).
- [32] C. T. Chubb and S. T. Flammia, *arXiv e-prints*, [arXiv:1809.10704](#) (2018), [arXiv:1809.10704 \[quant-ph\]](#).
- [33] S. T. Flammia and J. J. Wallman, in preparation (2019).
- [34] “Qiskit: An open-source framework for quantum computing,” (2019).
- [35] R. Harper and S. T. Flammia, *Phys. Rev. Lett.* **122**, 080504 (2019), [arXiv:1806.02359](#).
- [36] R. Harper, I. Hincks, C. Ferrie, S. T. Flammia, and J. J. Wallman, *Phys. Rev. A* **99**, 052350 (2019).
- [37] C. King and M. B. Ruskai, *IEEE Transactions on Information Theory* **47**, 192 (2001).
- [38] D. Gross, K. Audenaert, and J. Eisert, *J. Math. Phys.* **48**, 052104 (2007).
- [39] J. Wallman, *Quantum* **2**, 47 (2018), [arXiv:1703.09835](#).
- [40] A. Carignan-Dugas, J. J. Wallman, and J. Emerson, *Phys. Rev. A* **92**, 060302 (2015), [arXiv:1508.06312](#).
- [41] A. W. Cross, E. Magesan, L. S. Bishop, J. A. Smolin, and J. M. Gambetta, *npj Quantum Information* **2**, 16012 (2016), [arXiv:1510.02720](#).
- [42] A. K. Hashagen, S. T. Flammia, D. Gross, and J. J. Wallman, *Quantum* **2**, 85 (2018), [1801.06121](#).
- [43] R. Cleve, D. Leung, L. Liu, and C. Wang, *Quant. Inf. Comput.* **16**, 0721 (2016), [arXiv:1501.04592](#).
- [44] R. Harper and S. T. Flammia, *Quantum Science and Technology* **2**, 015008 (2017), [arXiv:1608.02943 \[quant-ph\]](#).
- [45] M. Cramer, M. B. Plenio, S. T. Flammia, R. Somma, D. Gross, S. D. Bartlett, O. Landon-Cardinal, D. Poulin, and Y.-K. Liu, *Nat Commun* **1**, 149 (2010), [arXiv:1101.4366](#).
- [46] B. P. Lanyon, C. Maier, M. Holzzapfel, T. Baumgratz, C. Hempel, P. Jurcevic, I. Dhand, A. S. Buyskikh, A. J. Daley, M. Cramer, M. B. Plenio, R. Blatt, and C. F. Roos, *Nature Physics* **13**, 1158 (2017), [arXiv:1612.08000](#).
- [47] Ł. Rudnicki, Z. Puchała, and K. Życzkowski, *Quantum* **2**, 60 (2018).

## Appendix A: Statistical Methods and Metrics.

**Analysis of probability distributions.** In the paper we use various metrics to analyse the probability distribution returned by the protocol. Here we formally define the terms we use. The *relative entropy*, also known as the Kullback-Leibler (KL) divergence, between two probability distributions is one measure, and is defined as

$$D(p||q) = \sum_j p(j) \ln \frac{p(j)}{q(j)}. \quad (\text{A1})$$

The *mutual information* is a measure of the dependence between two random variables  $X$  and  $Y$ , and it quantifies the amount of information obtained regarding one variable through observing the other. It is defined as:

$$I(X, Y) = D(p(x, y)||p(x)p(y)) \quad (\text{A2})$$

$$= \sum_{x,y} p(x, y) \ln \frac{p(x, y)}{p(x)p(y)}, \quad (\text{A3})$$

where  $D(p(x, y)||p(x)p(y))$  is the relative entropy between the joint probability distribution  $p(x, y)$  and the marginal distribution on each of the random variables.

For each run of the protocol, we have a partitioning of the set of 14 qubits into disjoint sets  $s$  that are acted upon by independent twirls. For each set  $s$  we define a random variable  $Q_s$  that takes on the value 0 if no error acts on the set  $s$  and 1 otherwise. For the single-qubit protocol, we have 14 random variables  $Q_0, \dots, Q_{13}$ . We then calculate the mutual information between each pair of random variables. For the two-qubit protocol, the set  $s$  comprises one or two qubits, depending on whether two-qubit gates were used on that pair or not.

*Conditional mutual information* represents the expected value of the mutual information of two random variables conditioned on the value of the third. In the present case we have:

$$I(X, Y|Z) = \sum_{z \in Z} p(z) \sum_{y \in Y} \sum_{x \in X} p(x, y|z) \log \left( \frac{p(x, y|z)}{p(x|z)p(y|z)} \right) \quad (\text{A4})$$

$$= \sum_{z \in Z, y \in Y, x \in X} p(x, y, z) \log \left( \frac{p(z)p(x, y, z)}{p(x, z)p(y, z)} \right). \quad (\text{A5})$$

One can use the probability distribution to compute the *covariance* matrix between the qubit Pauli error random variables. In the experiment presented in this paper, where we have averaged the Pauli errors, we can treat the qubits as 0/1 random variables representing no error/error. Then, if  $x$  is a column vector representing an error pattern, we compute the covariance matrix  $\Sigma$  as

$$\Sigma = \mathbb{E} [(x - \mu)(x - \mu)^T], \quad (\text{A6})$$

where  $\mu = \mathbb{E}[x]$  and  $\mathbb{E}$  denotes the expected value over the probability distribution.

Given the covariance it is simple to calculate the Pearson product-moment correlation coefficient matrix ( $Q$ ), obtained

by dividing the covariance of the two variables by their standard deviation. This is the *correlation matrix* plotted in the paper. In this case let  $V = \text{diag}(\Sigma)$ . Then we have:

$$Q = V^{-\frac{1}{2}} \Sigma V^{-\frac{1}{2}}. \quad (\text{A7})$$

In the case where one averages over the Pauli group (instead of the Clifford group) to characterise the Pauli noise of the device (rather than the basis-averaged Pauli noise of the device presented here in our experiments), then the relevant qubit random variable can be characterized by the  $2n \times 2n$  Pauli covariance matrix, where each row and column of the matrix is labeled by the  $2n$ -bit string required to label each of the  $\sigma_x$  and  $\sigma_z$  components of a single-qubit Pauli on  $n$  qubits.

One of the problems with the relative entropy  $D(p||q)$  is that it is defined only if  $\forall j, q(j) = 0 \implies p(j) = 0$  and this might not be the case in practice, especially when numerical precision issues are taken into account. For this reason we use the Jensen-Shannon distance (JSD) which is defined as:

$$\text{JSD}(p, q) = \left( \frac{1}{2}D(p||m) + \frac{1}{2}D(q||m) \right)^{1/2}, \quad (\text{A8})$$

where  $m(j) = (p(j) + q(j))/2$ . This is a smoothed, symmetric measure which always has a finite value and has the mathematical properties of a metric.

In [Figure 4](#) we use the *Hellinger distance*. The Hellinger distance forms a bounded metric on the space of probability distributions over a given probability space and, for discrete distributions, is defined as:

$$H(p, q) = \left( 1 - \sum_j \sqrt{p(j)q(j)} \right)^{1/2}. \quad (\text{A9})$$

This distance is efficient to compute and is related to the more commonly used but difficult to compute notion of *statistical distance* (or total variational distance)  $\delta(p, q)$  as:

$$H^2(p, q) \leq \delta(p, q) \leq \sqrt{2}H(p, q), \quad (\text{A10})$$

where

$$\delta(p, q) = \frac{1}{2} \sum_j |p(j) - q(j)|. \quad (\text{A11})$$

**Gibbs Random Fields.** A Gibbs random field (GRF) is an undirected graphical model of a set of random variables having the following property, known as the local Markov condition: Any subset of variables is conditionally independent of all other variables given its neighbors. Here the notion of adjacent is computed with respect to the factor graph of the model, as explained in the main text. That is, for a given subset  $A$  of random variables and a subset  $B$  containing the boundary  $\partial A$  of  $A$ , the following holds  $\Pr(x_A|x_B) = \Pr(x_A|x_{\partial A})$ , where  $x_A$  is the random variable describing the errors on the qubits in  $A$ .

For the current experiment we can use the topology of the device to define a Markov network, where the connections in the graph are identical to the resonators between the qubits.

The graph appears in [Figure 2](#). If we wish to enforce short-range correlations then we have:

$$\begin{aligned} p(0|1, 13, 2, 12, 3, 11, 4, 10, 5, 9, 6, 8, 7) &= p(0|1, 13) \\ p(1, 13|0, 2, 12, 3, 11, 4, 10, 5, 9, 6, 8, 7) &= p(1, 13|0, 2, 12) \\ p(2, 12|0, 1, 13, 3, 11, 4, 10, 5, 9, 6, 8, 7) &= p(2, 12|1, 13, 3, 11) \\ p(3, 11|0, 1, 13, 2, 12, 4, 10, 5, 9, 6, 8, 7) &= p(3, 11|2, 12, 4, 10) \\ \dots, & \end{aligned} \quad (\text{A12})$$

where we have used numbers to represent random variables, e.g. 0 for  $x_0$ , to de-clutter the notation.

We can then use the chain rule to write the joint probability distribution as follows:

$$\begin{aligned} p(0, 1, 13, 2, 12, 3, 11, 4, 10, 5, 9, 6, 8, 7) &= \\ p(0|1, 13, 2, 12, 3, 11, 4, 10, 5, 9, 6, 8, 7) &\times \\ p(1, 13|2, 12, 3, 11, 4, 10, 5, 9, 6, 8, 7) &\times \\ p(2, 12|3, 11, 4, 10, 5, 9, 6, 8, 7) &\times \\ \dots &\times \\ p(6, 8|7) &\times p(7) \end{aligned}$$

then using [Equation A12](#), this simplifies to:

$$p(0|1, 13)p(1, 13|2, 12)p(2, 12|3, 11) \dots p(6, 8|7)p(7)$$

which we can calculate as

$$\begin{aligned} \frac{p(0, 1, 13)}{p(1, 13)} &\times \frac{p(1, 13, 2, 12)}{p(2, 12)} \times \frac{p(2, 12, 3, 11)}{p(3, 11)} \\ \dots &\times \frac{p(6, 8, 7)}{p(7)} \times p(7). \end{aligned} \quad (\text{A13})$$

Finally we can use the probability distribution defined in [Equation A13](#) to reconstruct the *Gibbs random field*, that is, the probability distribution induced by the condition imposed by our chosen Markov conditions. A comparison between the observed probability distribution and the induced one by, say, the Jensen-Shannon distance gives us a metric to observe how closely our device corresponds to a device that only has short range correlations.

**IBM Quantum Experience.** The experiments reported here were conducted on the IBM Quantum Experience *Melbourne* device. Jobs were submitted via Qiskit [34] in two separate runs. The single qubit experiment consisted of 1,000 different submissions. Each submission contained 11 single-qubit Clifford twirls on each of the 14 qubits for gate lengths 1, 5, 10, 15, 20, 30, 45, 60, 75, 90, 105, with each gate length sequence requesting 1024 shots. This meant in total  $1024000 \times 11$  measurements were made. For step 4 of the protocol (see [Figure 1](#)) simple least squares fitting was used, although for any sequence length where the value was less than  $(p_1 + 1/16)/4$  that data and the data from longer sequences were discarded for the purposes of the fit.

With the two-qubit protocol the topology of the *Melbourne* device does not allow seven qubit pairs to be operated simultaneously. The qubits were grouped into six distinct qubit pairs, the remaining two qubits being operated in single-qubit-protocol mode. In order to determine which qubit pairs to

activate, attention was paid to the reported fidelities of the CNOT gates. For instance on 18 February 2019, the two-qubit gate between qubits 13 and 1 had a reported fidelity of 84.1% (other gates could be as high as 97%). The groupings shown in Figure 3 were chosen to attempt to ensure wide coverage of the various two-qubit gates available while avoiding any gates with a reported fidelity close to or below 90%. Only one of the three configuration settings is reported in the paper, the others appear in the appendices. Because of the possibility that correlations within the device might change with re-calibration all the different runs shown in Figure 3 were interleaved. In total there were 1924 different submissions (of 11 different sequence lengths) for each of the three different configurations. One re-calibration cycle did occur during the gathering of the data, although the fidelities of the two-qubit gates did not appear to change significantly as a result. The data does, however, represent an average of the noise that occurred in the machine during that time period. Given the reduced fidelity of the runs (since two-qubit gates have an infidelity of an order of magnitude greater than the single-qubit gates) sequence lengths were reduced to 0 . . . 10. The 0 sequence, representing one single qubit Clifford (i.e. no two-qubit gate), was added so as to allow a more accurate determination of the  $A$  constant in the fit. As with the single-qubit runs, data with a value less than  $(p_0 + 1/16)/4$  were discarded for the purposes of the fit, although a minimum of three data points were retained.

Finally in all cases an  $X$  gate was randomly compiled into the qubits of each sequence submitted, with the probability distribution interpreted accordingly so as to eliminate any bias in the SPAM [36].

**Error Bars.** All error bars shown here were calculated using non-parametric bootstrap methods. For each sequence length of each run the observed probability distributions of the measurement counts (Step 2 in the protocol shown in Figure 1) were re-sampled (with replacement) for the same number of measurements used to originally gather the data. This was repeated 1,000 times. Each of these 1,000 sets of re-sampled distributions were then analyzed in a manner identical to the original (steps 3, 4 and 5 of the protocol), to provide 1,000 bootstrapped samples of the SPAM free probability vector (the *bootstrapped probabilities*). From this the appropriate confidence intervals to provide error bars can be constructed. With the mutual information estimates the mutual information between the qubits in question can be calculated 1,000 times, ordered, and by extracting the values at the appropriate location of the ordered values, the confidence intervals are obtained (so for  $1\sigma$  confidence intervals the 159th and 841st values are used). With the error bars on the correlation matrices the following conservative approach was adopted. Using the bootstrapped probabilities, 1,000 correlation matrices were constructed. Since there is no clear way to order such matrices, each individual cell on the matrices was treated separately, with the possible values for that cell location being ordered and the appropriate high/low values being extracted as before. While a matrix constructed from all the low (or high) values would not in itself be a valid correlation matrix, it is believed the error bars still, conservatively, convey the confidence intervals for each of the individual values in the matrix. Finally

with the calculation of the Jensen-Shannon distance two different re-sampling techniques were utilized. In the first the Gibbs random field reconstructed probability distribution for the originally observed distribution was compared to each of the bootstrapped probability distributions and in the second an Gibbs random field distribution was constructed from each bootstrapped probability distribution and compared to the full bootstrapped distribution it was constructed from. In all cases the error ranges were broadly similar and in the paper the uncertainties quoted were taken from largest error ranges from either of the methodologies.

## Appendix B: Notation

### 1. Channels

We analyze noise as quantum channels, that is, as completely positive trace preserving (CPTP) linear maps  $\mathcal{L} : \mathbb{C}^{d \times d} \rightarrow \mathbb{C}^{d \times d}$ , mapping operators to operators. For  $n$  qubits, we have  $d = 2^n$ .

It is convenient to work in the superoperator representation of quantum channels. The superoperator representation is conveniently expressed in a trace-orthonormal operator basis. Here we will use the Pauli basis representation of a channel  $\mathcal{E}$ , which chooses the suitably normalized Pauli operators as the trace-orthonormal basis. Thus for the orthonormal basis  $\mathbb{A} = \{A_0, A_1, \dots, A_{d^2-1}\}$  we set  $A_0 = \mathbb{1}/\sqrt{d}$  which fixes the first operator as the one with a nonzero trace, all the others being traceless. For a single qubit the remaining 3 operators will be the  $X$ ,  $Y$  and  $Z$  Pauli operators respectively. For systems with a larger number of qubits the orthonormal basis is formed from the natural tensor products of these four Pauli operators, with  $A_0$  being the appropriately normalized  $\mathbb{1}^{\otimes n}$ , where  $n$  is the relevant number of qubits.

The superoperator representation of a quantum channel acts naturally via matrix multiplication on the vectorization of a density operator  $\rho$ , which we denote by  $|\rho\rangle$ . The notation  $|\rho\rangle$  simply indicates that  $\rho$  is now being treated as a vector whose components can be expanded in the above-mentioned orthonormal operator basis (in this case the Pauli basis). Concretely, we can expand the density operator as  $\rho = \sum_k \langle A_k, \rho \rangle A_k$ , where  $\langle A_k, \rho \rangle$  represents the Hilbert-Schmidt inner product  $\text{Tr}(A_k \rho)$  between the hermitian basis operator  $A_k$  and the density matrix  $\rho$ . Once we have done that we can identify  $\rho$  with the a column vector  $|\rho\rangle \in \mathbb{C}^{d^2}$  where the  $k^{\text{th}}$  entry is the relevant Hilbert-Schmidt inner product specified above. The superoperator representation of a channel  $\mathcal{E}$  is then the unique matrix  $\mathcal{E} \in \mathbb{C}^{d^2 \times d^2}$  such that  $\mathcal{E}|\rho\rangle = |\mathcal{E}(\rho)\rangle$ .

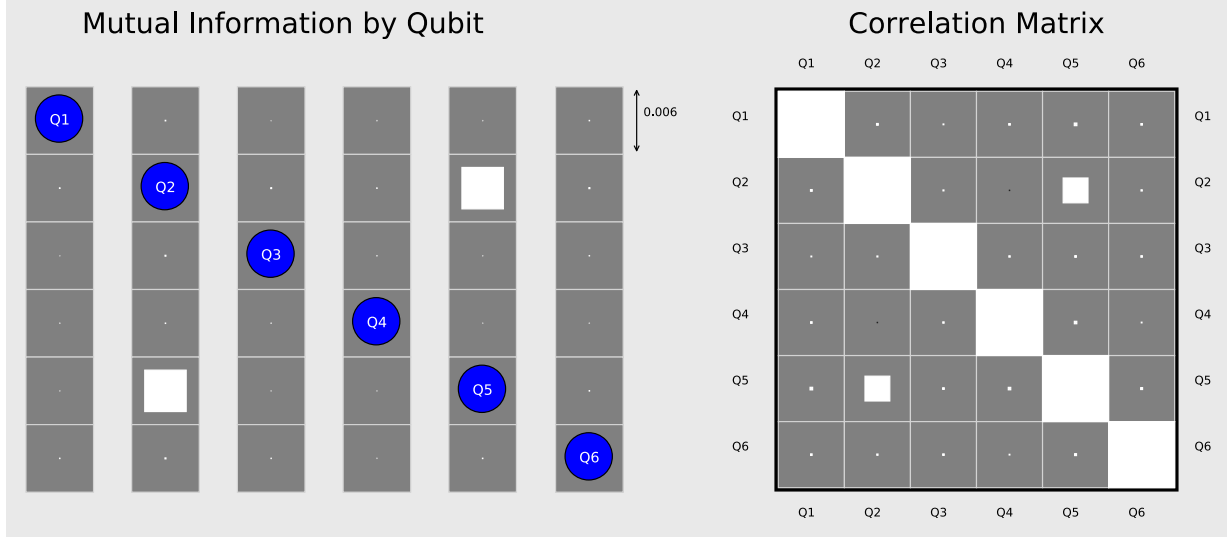
Where we have fixed  $A_0$  to be the rescaled identity operator then any CP channel  $\mathcal{E}$  can be written in block form as

$$\mathcal{E} = \begin{pmatrix} S(\mathcal{E}) & \mathcal{E}_{\text{sdl}} \\ \mathcal{E}_{\text{n}} & \mathcal{E}_{\text{u}} \end{pmatrix}, \quad (\text{B1})$$

where we refer to  $\mathcal{E}_{\text{sdl}}$ ,  $\mathcal{E}_{\text{n}}$  and  $\mathcal{E}_{\text{u}}$  as the *state-dependent leakage*, *nonunital* and *unital* blocks respectively (see [23])



(a)



(b)

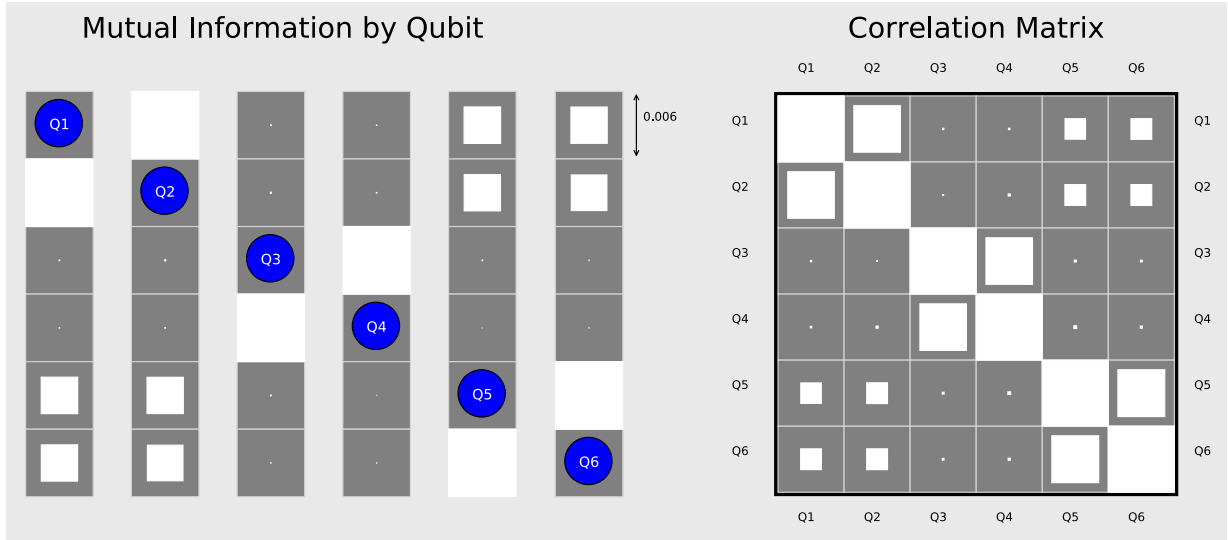


FIG. 5. Numerical simulation of a noisy 6 qubit system. Left hand plots show the mutual information between each identified qubit and the others via a Hinton diagram. Right hand plots show a correlation matrix identifying the correlations between each of the qubits. Relative size of white/black represents the strength of the mutual information/correlation, with the color white (black) being positive (negative). (a) The plots here arise from a simulation where the noise matrix is tensored single qubit noise with an additional two-qubit interaction between qubits 2 and 5. The protocol is operated in single qubit mode (see [section C 2](#)). As can be seen the protocol allows the identification of the correlation. (b) The system here has single-qubit noise applied to each qubit. The protocol is operated in ‘two-qubit’ mode ([section C 3](#)) with the qubits being paired as (1,2), (3,4) and (5,6). Each time a two-qubit gate is activated additional noise is applied to the qubits involved representing noisy two-qubit gates. Finally when the two-qubit gate between qubits 1 and 2 is activated further crosstalk noise is applied as between qubits 2 and 5 (representing crosstalk between the resonator between qubits 1 and 2 and the operation of qubit 5). Since errors are transmitted through the two-qubit gates of paired qubits there is significant mutual information and correlations between such qubits. The charts show the additional crosstalk (2 to 5) as mutual information (or correlations) between qubits 1,2 and 5,6. (The two-qubit operation spreads this error from 5 to 6). See [section C 4](#) for fidelity extraction.

for more details about this decomposition). If the channel is trace preserving then  $\mathcal{E}_{\text{sdl}} = 0$ . The unital block ( $\mathcal{E}_{\text{u}}$ ), and more precisely the diagonal of the unital block, contains all the information necessary to extract the Pauli noise afflicting

the system, including for instance the fidelity of the channel and/or the fidelity of any subspace of the system.

From this representation, the *Pauli projection* is the projection of the channel to just its diagonal entries (in the Pauli ba-

sis). In particular, this projection can be effected by *twirling* the channel with respect to the Pauli group, i.e., by averaging the noise channel as  $\mathcal{E}^{\mathcal{P}}(\cdot) := 4^{-n} \sum_j P_j \mathcal{E}(P_j \cdot P_j) P_j$ . The diagonal elements of  $\mathcal{E}$  or of the Pauli projection  $\mathcal{E}^{\mathcal{P}}$  are exactly the Pauli fidelities,  $f(j) = 2^{-n} \text{Tr}(P_j \mathcal{E}(P_j))$ .

When the noise channel is twirled by the Clifford group, the resultant noise channel will also have  $\mathcal{E}$  diagonalized in the Pauli basis, with each element being the average of the diagonal elements of the original  $\mathcal{E}_u$ . By way of illustration in the single-qubit case, a completely positive trace preserving noise channel will be of the form:

$$\mathcal{E} = \begin{pmatrix} 1 & 0 & 0 & 0 \\ \alpha_1 & f_x & \delta_1 & \delta_2 \\ \alpha_2 & \delta_3 & f_y & \delta_4 \\ \alpha_3 & \delta_5 & \delta_6 & f_z \end{pmatrix} \quad (\text{B2})$$

where all the elements are real. The matrix elements themselves obey certain constraints on account of the requirement for complete positivity; see Ref. [37] for an explicit description of these constraints. In particular we note that where the noise is purely decoherent all  $\delta_i = 0$ , where  $i = \{1..6\}$ , whereas if the noise is coherent the sum of the square of each element of  $\mathcal{E}_u = d^2 - 1$ , which = 3 for a single qubit. We will make explicit use of the parameters  $f_x, f_y$ , and  $f_z$  below.

After averaging over the Clifford group, the unital block  $\mathcal{E}_u$  of the twirled error channel looks like

$$\begin{pmatrix} \frac{1}{3}(f_x + f_y + f_z) & 0 & 0 \\ 0 & \frac{1}{3}(f_x + f_y + f_z) & 0 \\ 0 & 0 & \frac{1}{3}(f_x + f_y + f_z) \end{pmatrix}. \quad (\text{B3})$$

If the average were over the Pauli group, the unital block would be:

$$\begin{pmatrix} f_x & 0 & 0 \\ 0 & f_y & 0 \\ 0 & 0 & f_z \end{pmatrix}. \quad (\text{B4})$$

The standard randomized benchmarking protocol twirls the noise through the Clifford group, meaning that the depolarizing factor measured by it (the decay rate), is simply  $\frac{1}{3}(f_x + f_y + f_z)$ .

More generally, RB over the full Clifford group will learn the decay parameter  $\bar{f} := \frac{1}{d^2-1} \sum_{j \neq \mathbb{1}} f_j$ . The number typically reported by experiments, however, is the closely related notion of *average gate fidelity*  $\mathcal{F}$ , which is a shifted and rescaled version of this given by  $\mathcal{F} = \frac{(d-1)\bar{f}+1}{d}$ . Some experiments report instead the average gate *infidelity* or *average error rate*  $r$ , which is just  $r = 1 - \mathcal{F} = \frac{d-1}{d}(1 - \bar{f})$ .

When we have a Pauli-projected noise matrix we will refer to each of the diagonal entries in the matrix as a **decay parameter**, which we will typically denote as  $f$ . These are also known as the Pauli fidelities. Unless otherwise clear by the context,  $f_x, f_y, f_z$ , will refer to the  $f$  parameters associated with the specific sub-scripted Pauli channel, whereas  $f_\Sigma$  will typically refer to an  $f$  parameter associated with an averaged noise channel, such as in eq. (B3).

## 2. Measurement

In the superoperator representation, a projective measurement is represented by a row vector for the projection operator expanded in the Pauli basis. So, for instance, in a two qubit system if we were to prepare and measure in the computational basis the entries would relate to the Pauli operators,  $II, IZ, ZI$ , and  $ZZ$ . Assuming each qubit is measured separately we can use  $\uparrow$  to represent an ‘up’ and  $\downarrow$  a ‘down’. We then have four different possible measurement outcomes  $\uparrow\uparrow, \uparrow\downarrow, \downarrow\uparrow$  and  $\downarrow\downarrow$ . The following relationship holds:

$$\begin{aligned} \uparrow\uparrow &= \begin{pmatrix} II : + \\ IZ : + \\ ZI : + \\ ZZ : + \end{pmatrix}, & \uparrow\downarrow &= \begin{pmatrix} II : + \\ IZ : - \\ ZI : + \\ ZZ : - \end{pmatrix}, \\ \downarrow\uparrow &= \begin{pmatrix} II : + \\ IZ : + \\ ZI : - \\ ZZ : - \end{pmatrix}, & \downarrow\downarrow &= \begin{pmatrix} II : + \\ IZ : - \\ ZI : - \\ ZZ : + \end{pmatrix}. \end{aligned} \quad (\text{B5})$$

By inspection we can see that the (properly normalized) sum of the above gives the identity (i.e. we are asserting that the qubits will always be in one of these four states). More importantly we can rearrange the above to note that:

$$\begin{aligned} II &= \uparrow\uparrow + \downarrow\uparrow + \uparrow\downarrow + \downarrow\downarrow \\ IZ &= \uparrow\uparrow + \downarrow\uparrow - \uparrow\downarrow - \downarrow\downarrow \\ ZI &= \uparrow\uparrow - \downarrow\uparrow + \uparrow\downarrow - \downarrow\downarrow \\ ZZ &= \uparrow\uparrow - \downarrow\uparrow - \uparrow\downarrow + \downarrow\downarrow. \end{aligned} \quad (\text{B6})$$

In other words we can reconstruct the relevant entries in a vectorized state if we know the percentage chance of each of the four different measurement outcomes. Clearly such outcomes will only be known approximately and we discuss later how to deal with this and how to relate the values to the relevant noise channel acting on a noisy state.

As shown in Ref. [33] the relationship detailed in eq. (B6) is an inverse Walsh-Hadamard transform from the observed probability distribution to the relevant values of the noise matrix generating such a distribution. This relationship generalizes to  $n$ -qubits. Accordingly, given the probability distribution of observed outcomes over  $n$ -qubits one can perform a Walsh-Hadamard transform to determine the relevant entries in the state that produced them.

## 3. Clifford subsystem twirling

As noted in [38], any unitary 2-design, which in particular includes the Clifford group, has exactly 2 irreducible representations (**irreps**) in its matrix representation in the superoperator representation.

Given a representation  $(\phi, V)$  defined by a homomorphism  $\phi$  and a vector space  $V$  for a group  $\mathfrak{G}$  and a matrix  $A \in \text{GL}(V)$ , we define an action (the *twirl*)

$$A^g = \phi(g) A \phi(g^{-1}), \quad (\text{B7})$$

where  $g^{-1}$  is the inverse of  $g$ . We can do this for each element of  $\mathfrak{G}$ , which gives us the uniform average of this action defined as:

$$A^G = \frac{1}{|\mathfrak{G}|} \sum_{g \in \mathfrak{G}} A^g, \quad (\text{B8})$$

where  $|\mathfrak{G}|$  is the number of elements in the group. The important thing to notice here is that  $A^G$  commutes with the action of  $\mathfrak{G}$  for any representation  $(\phi, V)$ . Schur's Lemma for algebraically closed fields provides that if  $(\phi, V)$  is a finite-dimensional irrep and  $f$  is an intertwining operator, then  $f = \lambda \mathbb{1}$  for some scalar  $\lambda$ . In this case the action  $A^G$  commutes with all representations and therefore is an intertwining operator. In the case that the decomposition into irreps of a given representation is multiplicity-free, then the twirling operation makes any operator especially simple. When a 'twirl' is performed by averaging the noise matrix by the action of the group with such a multiplicity-free representation, the noise matrix in the superoperator basis is reduced to a diagonal matrix with the number of distinct entries equal to the number of irreducible representations of the twirling group.

For instance with a single qubit the noise matrix will have one parameter representing the trivial irrep (which will always be 1 for a quantum channel), with the second irreducible representation diagonalizing the matrix as shown in eq. (B3). In general where a subsystem is twirled by the full Clifford group (or, indeed, any unitary 2-design) corresponding to that subsystem, there are two irreducible sub-spaces corresponding to the two stabilized projectors,  $\Pi_o$  (the trivial/identity operator) and a projector  $\Pi_f$ , being a projector onto the remainder of the Pauli group acting on those qubits. As shown in [26], when we twirl over two distinct groups of subsystem Clifford operators (i.e. a  $\mathcal{C}^{\otimes 2}$  twirl) we obtain four distinct irreducible sub-spaces  $\Pi_0 = \mathbb{1} \otimes \mathbb{1}$ ,  $\Pi_2 = \mathbb{1} \otimes \Sigma$ ,  $\Pi_1 = \Sigma \otimes \mathbb{1}$  and  $\Pi_{12} = \Sigma \otimes \Sigma$ , where  $\Sigma$  is the vector of Pauli operators for each subsystem. The size of each of the irreducible representations can be calculated from the character  $\chi$  of the underlying irreducible representations. In the case of a single qubit Clifford twirl this is  $\chi_{\mathbb{1}} = 1$ ,  $\chi_{\Sigma} = 3$  and so for a  $\mathcal{C}^{\otimes 2}$  we have:

$$\chi_{\mathbb{1} \otimes \mathbb{1}} = 1 \times 1 = 1 \quad (\text{B9})$$

$$\chi_{\Sigma \otimes \mathbb{1}} = 3 \times 1 = 3 \quad (\text{B10})$$

$$\chi_{\mathbb{1} \otimes \Sigma} = 1 \times 3 = 3 \quad (\text{B11})$$

$$\chi_{\Sigma \otimes \Sigma} = 3 \times 3 = 9. \quad (\text{B12})$$

This generalizes in the obvious way to twirls over  $n$  qubits, where if there is a single Clifford twirl over each qubit, there will be  $2^n$  irreducible representations with multiplicities given by simple multiplications of the characters.

Importantly in an  $n$ -qubit system where each qubit is independently twirled over the Clifford group, each irrep is of the form  $\{\mathbb{1}, \Sigma\}^{\otimes n}$  and therefore each  $\{I, Z\}^{\otimes n}$  Pauli belongs to one (and exactly one) of the irreps and the associated decay parameter (in the case of a twirled noise channel). To keep the notation as simple as possible where we refer to the decay parameter of these averaged channels with a  $\Sigma$  in the appropriate place, omitting the  $\otimes$  notation. So for a two qubit system,

twirled with two independent Clifford twirls, the following holds:

$$f_{II} = f_{II} \quad (\text{B13})$$

$$f_{\Sigma I} = \frac{1}{3}(f_{XI} + f_{YI} + f_{ZI}) \quad (\text{B14})$$

$$f_{I\Sigma} = \frac{1}{3}(f_{IX} + f_{IY} + f_{IZ}) \quad (\text{B15})$$

$$f_{\Sigma\Sigma} = \frac{1}{9}(f_{XX} + f_{XY} + f_{XZ} + f_{YX} + f_{YY} + f_{YZ} + f_{ZX} + f_{ZY} + f_{ZZ}) \quad (\text{B16})$$

To summarize, if we have an  $n$ -qubit system and we perform a single-qubit Clifford twirl on each of the qubits, we diagonalize the noise matrix ( $4^n \times 4^n$  superoperator) representing the average difference between the noisy gates and their ideal counterparts [39] into a matrix that has  $2^n$  different diagonal entries. Furthermore, each entry is associated with a value that we can determine from the probabilities of measuring each qubit in the computational basis (see appendix B 2).

## Appendix C: Learning the averaged noise

### 1. Randomized Benchmarking

Here we recap the relevant parts of the randomized benchmarking protocol.

The *raison d'être* of randomized benchmarking is to allow small error rates to be measured in a way that is robust to state preparation and measurement (SPAM) errors in the device being characterized. It does this by using a Clifford twirl (discussed earlier) to transform the noise into a depolarizing channel with the same fidelity as the noise being twirled. At the end of each sequence a final inverting gate is applied (which would in an ideal system return the state of the system to its initial state). One way of looking at this is that it allows a distribution relating to the probability of the state returning to the intended state to be sampled and the underlying percentages to be estimated in a SPAM-free manner. Given this, the typical randomized benchmarking protocol becomes:

1. Choose a positive integer  $m$ .
2. Choose a random sequence of gates  $s$  from a set  $\mathbb{S}_m$ , typically of Clifford gates. Note that in modern versions of this protocol these gates are chosen randomly to either leave the state invariant or to map it to an orthogonal state in order to eliminate a nuisance model parameter (see e.g. Ref. [36]).
3. Obtain an estimate  $\hat{q}(m, s)$  of the expectation value  $q(m, s)$  of an observable  $E$  after preparing a state  $\rho$  and applying the gates in  $s$ .
4. Repeat steps 2–3 to obtain an estimate  $\hat{q}(m)$  of  $\bar{q}(m)$ .

5. Repeat steps 1–4 and fit to the model

$$\bar{q}(m) = Ac^m + B \quad (\text{C1})$$

where  $c$  is related to some parameter of interest (e.g., the average gate fidelity to the identity) and  $A$  is a SPAM-dependent constants and  $B$  is a constant that varies with the number of qubits.

This protocol provably works well when there is one dominant decay parameter that needs to be ascertained. When multiple parameters need to be known the difficulty of fitting multiple decay parameters is mitigated by preparing particular states (or applying particular gates) that will maximize one of the pre-factors while minimizing the others (e.g. [26, 40–42]) or using projective properties of subgroups of the relevant groups [24]. To date, in all cases where multiple parameters need to be found a number of different experiments need to be run to ascertain the fitting parameters. Despite the difficulty of this, in practice it has been shown to be successful (e.g. Ref. [35]).

## 2. Protocol to measure all the single-qubit $f$ parameters simultaneously

The idea of the protocol is that rather than using different types of experiments to extract multiple  $f$  parameters one at a time, we can use the probability distribution of independent measurements on each qubit to reconstruct the relevant  $\{\mathbb{1}, Z\}^{\otimes n}$   $f$  parameters  $f_i$ , ( $i \in \{1..2^n\}$ ), corresponding to the  $2^n$  irreps related to single-qubit Clifford twirls conducted simultaneously on each qubit. In the next section we will also discuss how to generalize this to the case where we use a multi-qubit Clifford group.

We can measure all  $2^n$  qubit error rates by performing an inverse Walsh-Hadamard transform on the  $2^n$  different possible  $\{\uparrow, \downarrow\}^{\otimes n}$  observation outcomes (see appendix B 2) to determine the  $f$  parameters that lead to such measurement outcomes. For twirled channels, the observed probability distributions will be caused by a combination of both the SPAM and the  $f$  parameters associated with the noisy gates. We want to be able to isolate the  $f$  parameters. By estimating the decay parameter (being the combination of both SPAM and gate noise) at varying gate lengths ( $m$ ), we can fit each of these parameters to a formula of the form  $Ap(j)^m$ , eliminating SPAM noise and (with appropriately chosen  $m$ ), ensuring the error in our estimates are multiplicative in  $1 - f$  for each of the  $f$  being estimated [33, 36]. Once we have SPAM-free estimates of the  $f$  values, we can again use a Walsh-Hadamard transform to reconstruct the SPAM-free estimate of the probability distribution of qubit error rates in the machine. This has many uses, some of which we detail later.

More precisely, the protocol for an  $n$  qubit system is as follows:

1. Choose a positive integer  $m$ .

2. Choose a random sequence of gates  $s$  from a set  $\mathbb{S}_m$ , drawn from the one-qubit Cliffords for each qubit. For each qubit sequence, choose the gates randomly to either leave the state of that qubit invariant or to map it on an orthogonal state.
3. Obtain an estimate  $\hat{q}(m, s)$  of the probability distribution over the  $2^n$  different measurement outcomes for the the  $n$  observables (being the measurement of each the  $n$  qubits in the device).
4. Repeat steps 2–3 to obtain an estimate  $\hat{q}(m)$  of  $\bar{q}(m)$ , ( $\hat{q}(m)$  being a vector with  $2^n$  entries one for each of the possible observed outcomes).
5. Transform  $\hat{q}(m)$  by applying the Walsh-Hadamard transformation to obtain  $\hat{p}(m)$  representing the estimate of the relevant entry in the noise matrix (applied to itself  $m$  times).
6. Repeat steps 1–5 and then for each parameter in fit  $\hat{p}(m)$  fit to the model

$$\bar{p}(m) = Ap^m \quad (\text{C2})$$

to obtain SPAM free estimates of the relevant decay parameters.

7. Use the relevant estimates of the decay parameters (with a forward Walsh Hadamard transform) to reconstruct the entire probability distribution, if necessary projecting onto a simplex to ensure all probabilities are  $\geq 0$ .

Note that depending on the data required and the size of the system it is perfectly acceptable to marginalize the data for Steps 5 and 6 before fitting, rather than fitting all the data, converting back to probabilities and then marginalizing. The Walsh-Hadamard transform and the marginalization of probabilities commute and one can choose whichever route is easier. However, this is not the case with the final projective step onto the probability simplex.

## 3. Protocol to measure sets of two-qubit $f$ parameters simultaneously

The protocol discussed in appendix C 2 relied on single-qubit Clifford gates to average the Pauli noise. In many architectures the noise on two-qubit gates is quite different from that of single-qubit gate noise. Here we present an extension to a protocol that allows the characterization of the noise in the system where such qubit-to-qubit couplings are used.

In order to activate such two-qubit couplings a two-qubit randomized benchmarking protocol can be conducted between qubit pairs. The easiest way is just to use two-qubit randomized benchmarking. The number of Cliffords to choose from is relatively small (11,520 gates), and can be reduced further using, for example, the group identified in [43] (960 gates).

The protocol is otherwise identical. However, it should be noted that errors in one qubit will now spread to the other

qubit involved in the two-qubit gate, thus their errors will be correlated when the probability distributions are analyzed (see later). Finally, when qubits have multiple qubits with which they can interact, the protocol only allows one such link to be tested at a time. The two-qubit gates need to be placed into distinct sets. If one wishes to analyze every two-qubit link then the number of such sets (and thus the number of times the protocol will need to be repeated) is equal to the number of connections of the most connected qubit, which given current devices will be a manageable number.

It should be noted, however, that the average number of two-qubit gates in a full two-qubit Clifford twirl is not insignificant (using only, say a controlled- $Z$  gate ( $C_Z$ ), it has an average of approx 1.6, with a maximum of 3) and when all the qubits are active at once this may lead to decay rates that are too large to be measured accurately (i.e. they decay to the maximally mixed state with just a few gates).

If one desires to have all the two-qubit gates acting at the same time one could use the protocol given in Ref. [24], interleaving a two-qubit gate such as the  $C_Z$  gate between two single qubit Clifford twirls. However, it should be noted that with low gate numbers, one only gets an approximate exponential decay rate. Where we use a Paul twirl instead of a Clifford twirl this non-exponential decay rate does not arise, but then we do not average the Pauli noise, increasing the number of parameters we need to measure.

Alternatively, we can adapt the twirl outlined in [44] and perform a  $\mathcal{C}C_Z\mathcal{P}C_Z$  twirl, where  $\mathcal{C}$  is a gate drawn from the group composed of single-Clifford twirls on two qubits,  $C_Z$  is the two-qubit gate and  $\mathcal{P}$  is one of the 16 two-qubit Paulis. Here we are using the fact that the two-qubit Clifford gate being, by definition, a Clifford gate, conjugates Paulis to Paulis. The protocol thus averages all the noise as described before except in this case it is the average of the square of each of the entries of the ‘noise matrix’ rather than just the average of the relative entries. As discussed in Ref. [44] the difference in the value of these figures is related to the anisotropy of the noise. Finally we note that the twirls in cycle benchmarking [25] can always be used to ascertain the Pauli noise in the device with interleaved two-qubit gates.

#### 4. Extracting the fidelity

It should be noted that the fidelity of the various noise models can be reconstructed trivially from the estimates in step 6 above, recalling that the average gate fidelity is  $\mathcal{F} = \frac{(d-1)\bar{f}+1}{d}$ , where  $\bar{f}$  is the average of the non-identity diagonal elements of the superoperator representing the noise. If a set of gates other than the Cliffords is chosen in step 2, then, depending on the group chosen, it will be possible to extract  $2^n$  parameters of interest per run. For instance, the real Cliffords [42] (of interest, for example, for codes that might not have a fault-tolerant phase gate [35]) when used as the twirling group gives three decay parameters. With the correct preliminary state (or initial gates) all decay parameters reside on one of the  $f_{\{I,Z\}}$  parameters extracted, allowing the fidelity to be calculated without the need for multiple different types of ex-

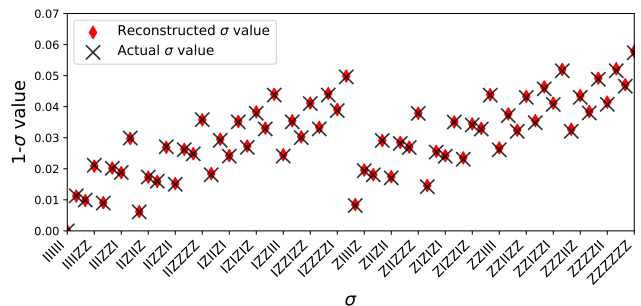


FIG. 6. Numerical simulation with a reconstruction of the 64 averaged elements of the 6 qubit noise matrix on the simulated system. Even with relatively few sequences (50) over just 11 different gate lengths, the relative error in any of the reconstructed 64 entries is less than 2%.

periments.

Because of the ability to transform the decay parameters (the  $f$  values) to a probability distribution (and vice-versa), when only subsets of the qubits are of interest the relevant decay parameters for such subsets are easily obtainable by converting to a probability distribution, marginalizing, and then converting back.

#### Appendix D: Scalable Estimations

As discussed in the main text, as the number of qubits being considered increases it will no longer be feasible to reconstruct the entire probability distribution of qubit error rates or Pauli error rates (the probability distribution itself growing exponentially with the number of qubits). However, reconstruction of covariance matrices and, more importantly, a Gibbs random field (GRF) decomposition, will remain scalable and can be conducted in polynomial time. The Walsh-Hadamard transform commutes with marginalizing the data, thus we can marginalize at the experiment level, transform, fit the data, and transform back to compute all relevant marginal joint probability distributions. In the limit of infinite data, this is identical to fitting all the data and then marginalizing the resulting probability distribution.

Using this technique will allow all covariances or correlations between the qubit to be determined in scalable way. This holds similarly for the case of Gibbs random field decompositions, where such decompositions will be motivated by the physical layout of the device.

When we have limited measurements and thus statistical fluctuations in the gathered data, the relevant marginals may differ from those that would be obtained from a consistent global probability distribution. For example, given three random variables  $A$ ,  $B$ , and  $C$ , and a global distribution  $p(A, B, C)$ , the estimated marginals will not generally obey simple self-consistency conditions that must hold for the full distribution, for example  $p(b) = \sum_a p(a, b) = \sum_c p(b, c)$ . The estimation of a globally consistent GRF and a bound on the error incurred at this step have been bounded in [33]. A

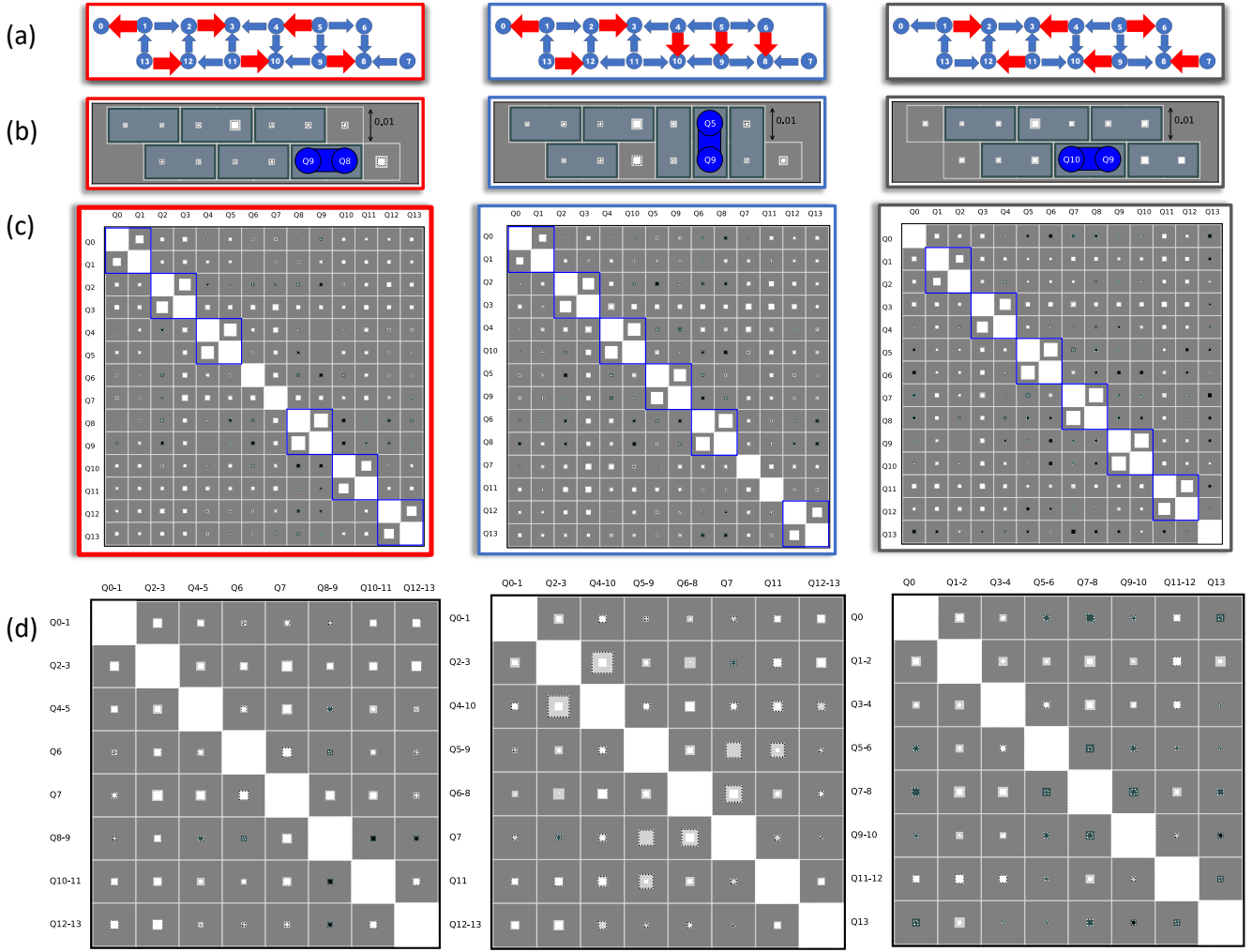


FIG. 7. (a) Schematic showing the activated two-qubit gates (in red) for each of the three protocols. (b) Hinton diagrams showing the mutual information between the highlighted qubit pairs and each of the other qubits. The darker shading in the diagrams indicates which qubits were operated in two qubit mode. The area of the white square indicates the strength of the mutual information. (c) The covariance matrices for each of the three protocols. The qubits that formed part of the two-qubit Clifford twirl are outlined in blue. Note in the second column the order of the qubits has been changed to ensure that qubits that are part of a two-qubit twirl are next to each other. (d) The covariance matrix where each of the qubits forming part of a two-qubit twirl are treated as a single random variable. This allows the correlations between these qubit pairs and the other qubit pairs to be seen more clearly.

similar technique can be used with the marginalised data to determine the parameters of the GRF decomposition being used to model the underlying probability distribution. Thus within the ansatz of the GRF decomposition the probability distribution can be learned within polynomial time up to an overall normalizing factor, assuming that the GRF has bounded degree.

In the present manuscript, the  $2^{14}$  values required for estimation of the qubit error rates are easily manipulated by current computers and the reconstructed probability distribution (with possible negative values) was projected onto the nearest (in Euclidean distance) point in the probability simplex. When such a brute-force manipulation is not possible, we need to determine the best consistent estimator for the reconstruction of the global covariance matrix from the (possi-

bly non-consistent) marginalized covariance matrices.

It is an open question what is the best method of covariance matrix estimation in the context of learning SPAM-free effective qubit or Pauli error rates. It is also open if methods analogous to the case of matrix product state learning [45, 46] can be generalized to quantum channels in a provable way. Such a result would be quite analogous to the GRF decomposition, but would allow for the modeling of more general quantum noise sources.

#### Appendix E: Running the protocol in simulation and on a device

For the purposes of demonstrating the effectiveness of the protocol we simulated a six-qubit system with two different

styles of noise and both the single-qubit protocol (section C 2) and the two-qubit protocol (section C 3). The noise models are described in some detail in the caption of Figure 5: we generate arbitrary high-fidelity single qubit noise using the techniques described in [47], and two-qubit noise is modeled as additional small controlled-qubit rotations between relevant qubits.

In the single-qubit protocol the noise is simply modeled as a superoperator noise matrix applied after each application of the six single-qubit gates. The noise matrix in the superoperator basis is, in this case, a  $4^6 \times 4^6$  matrix. The protocol allows the extraction of the  $2^6$  averaged  $f$  values from the total  $2^{12}$  diagonal values comprised in the noise matrix and the reconstruction of the actual probability distributions over the  $2^6$  possible measurement outcomes. For this the simulation sequence lengths of 1, 3, 5 up to 22 gates were measured, with each length having 50 different sequences, 8096 shots being taken for each sequence. As can be seen in Figure 6 even with this limited number of sequences this allowed an accurate reconstruction of the diagonal elements of the noise matrix (the relative error in each element was no more than, and often much less than, 2%). This would allow the fidelities of any of the qubits or collection of qubits to be read off with high accuracy. The pattern of fidelity  $f$  values in the chart reflects the higher noise on qubits 2 and 5.

Similarly with the two-qubit protocol, save that there will only be about  $2^{\frac{n}{2}}$  values to extract since the two-qubit twirl only has two irreps over a pair of qubits, the respective en-

tries in the reconstructed noise map could be averaged for increased accuracy.

#### Appendix F: Two-qubit protocol on the 14-qubit architecture

As discussed in the main paper, the two-qubit protocol was executed for three different patterns of activation of two qubit gates. Figure 7 shows the results of all three experiments and the correlation matrices extracted from the obtained data. Strikingly, it can be seen that in all cases qubit 3 became strongly correlated with all the other qubits in the machine once the two-qubit gates (and the time delays related to the use of two-qubit gates) were implemented. As discussed in the main paper, the JSD between the probability distribution measured using the the two-qubit protocol and the local GRF model has increased by almost an order of magnitude. For each of the layouts shown they are: 0.265(1), 0.271(3) and 0.245(2), respectively. Finally we note that in the correlation matrices there are some differences in the correlations between qubits (j,l) and (k,l) where (j,k) are operated as a two-qubit twirl. This implies that in such cases decay rates that should be identical because of the two-qubit twirl are empirically distinct. While the cause for this is left for future work, it is interesting that the protocol is able to highlight such matters.